Nanoimprinting for high-throughput replication of geometrically precise pillars in fused silica to regulate cell behavior

Ganjian, Mahya; Modaresifar, Khashayar; Rompolas, Dionysios; Fratila-Apachitei, Lidy E.; Zadpoor, Amir A.

DOI
10.1016/j.actbio.2021.12.001

Publication date
2022

Document Version
Final published version

Published in
Acta Biomaterialia

Acta Biomaterialia 140 (2022) 717–729

Contents lists available at ScienceDirect

Acta Biomaterialia

journal homepage: www.elsevier.com/locate/actbio

Full length article

Nanoimprinting for high-throughput replication of geometrically precise pillars in fused silica to regulate cell behavior

Mahya Ganjian*, Khashayar Modaresifar[1], Dionysios Rompolas[1], Lidy E. Fratila-Apachitei, Amir A. Zadpoor

Department of Biomechanical Engineering, Faculty of Mechanical, Maritime, and Materials Engineering, Delft University of Technology, Mekelweg 2, 2628CD, Delft, the Netherlands

ARTICLE INFO

Article history:
Received 30 August 2021
Revised 4 November 2021
Accepted 1 December 2021
Available online 5 December 2021

Keywords:
Thermal nanoimprint lithography
Soft lithography
Electron beam lithography
Osteogenic patterns

ABSTRACT

Developing high-throughput nanopatterning techniques that also allow for precise control over the dimensions of the fabricated features is essential for the study of cell-nanopattern interactions. Here, we developed a process that fulfills both of these criteria. Firstly, we used electron-beam lithography (EBL) to fabricate precisely controlled arrays of submicron pillars with varying values of interspacing on a large area of fused silica. Two types of etching procedures with two different systems were developed to etch the fused silica and create the final desired height. We then studied the interactions of preosteoblasts (MC3T3-E1) with these pillars. Varying interspacing was observed to significantly affect the morphological characteristics of the cell, the organization of actin fibers, and the formation of focal adhesions. The expression of osteopontin (OPN) significantly increased on the patterns, indicating the potential of the pillars for inducing osteogenic differentiation. The EBL pillars were thereafter used as master molds in two subsequent processing steps, namely soft lithography and thermal nanoimprint lithography for high-fidelity replication of the pillars on the substrates of interest. The molding parameters were optimized to maximize the fidelity of the generated patterns and minimize the wear and tear of the master mold. Comparing the replicated feature with those present on the original mold confirmed that the geometry and dimensions of the replicated pillars closely resemble those of the original ones. The method proposed in this study, therefore, enables the precise fabrication of submicron- and nanopatterns on a wide variety of materials that are relevant for systematic cell studies.

Statement of significance

Submicron pillars with specific dimensions on the bone implants have been proven to be effective in controlling cell behaviors. Nowadays, numerous methods have been proposed to produce bio-instructive submicron-topographies. However, most of these techniques are suffering from being low-throughput, low-precision, and expensive. Here, we developed a high-throughput nanopatterning technique that allows for control over the dimensions of the features for the study of cell-nanotopography interactions. Assessing the adaptation of preosteoblast cells showed the potential of the pillars for inducing osteogenic differentiation. Afterward, the pillars were used for high-fidelity replication of the bio-instructive features on the substrates of interest. The results show the advantages of nanoimprint lithography as a unique technique for the patterning of large areas of bio-instructive surfaces.

1. Introduction

The rapid expansion of cell-based therapies in a variety of pathological circumstances [1–3] along with the emergence of recent generations of cell-instructive biomaterials [4] have underscored the importance of directing the (stem) cell fate. While stem cells demonstrate an extensive capacity for commitment to certain lineages in response to many biochemical and/or biophysical exogenous stimuli [5,6], the complications associated with the use of biochemical agents, such as the high cost of growth factors and their potential adverse effects [7–9], have motivated researchers to

* Corresponding author.
E-mail address: m.ganjian@tudelft.nl (M. Ganjian).
[1] Equal contribution.

https://doi.org/10.1016/j.actbio.2021.12.001

investigate the physical interactions of cells and biomaterials to a deeper extent.

Among such physical stimuli, submicron and nanoscale topographies have been demonstrated to be particularly effective in controlling such cell behaviors as proliferation, migration, and differentiation [10–12]. While many studies have been carried out to elucidate the biological effects of surface patterns at the nanoscale (below 100 nm) [13–16], less is known about the optimum dimensions at the submicron scale (100-1000 nm) [6,17–19] for inducing specific cell responses.

Despite much effort dedicated to understanding the effects of surface topography on the various types of cell behavior, many aspects of such interactions remain poorly understood. One of the main reasons underlying this lack of understanding is the large number of design parameters that define the geometry and arrangement of such topographies. Each of those design parameters may influence the cell response in a unique way both in isolation and in combination with other design parameters. Moreover, the intracellular pathways by which the cells sense and respond to their microenvironment are highly complex [7,13,20]. There is, therefore, a need for extensive systematic studies to understand the effects of different design parameters on the interactions between submicron and nanoscale surface patterns and cell behavior. Such systematic studies are, however, hampered by practical considerations regarding the nanofabrication techniques. The currently available techniques for the fabrication of precisely controlled submicron and nanoscale patterns include electron beam-induced deposition (EBID) [21–23], electron beam lithography (EBL) [24,25], two-photon polymerization [26], etc. All of these techniques suffer from a major limitation, namely low throughout. A low throughput means that it is infeasible to pattern large surface areas. Some other techniques are available for high throughput patterning of surfaces at the nanoscale and submicron scales, including reactive ion etching [27,28], anodizing [29], and hydrothermal treatment [30–32]. These high throughput techniques, however, offer limited geometrical precision and usually lack the capability to change each design parameter independent from the others. There is, therefore, an urgent need for high throughput yet precise nanofabrication technique for the patterning of bio-instructive surfaces at the submicron and nanoscales. Nanoimprint lithography (NIL) is a facile fabrication technique that offers a number of unique advantages, including high throughput and scalability [33,34], the ability to pattern a large variety of geometrical features and materials with ultrahigh resolutions [35], simplicity, and low cost [36]. Given these favorable properties, NIL is widely used for the fabrication of biosensors [37,38], photovoltaics [39,40], bactericidal [7,41] and osteogenic nanopatterns [13,42–44], and flexible electronics [45–47].

Here, we use a combination of EBL and NIL for high throughput patterning of bio-instructive surfaces with geometrically precise submicron pillars. Variations in the interspacing of submicron pillars fabricated by two-photon polymerization have been recently shown to induce osteogenic differentiation in preosteoblasts [6]. The settling state of the cells on the pillars and traction forces applied to the pillars resulting in their tips to be displaced were hypothesized to determine the long-term osteogenic response of the cells. Nevertheless, the relatively low stiffness of the pillars could be a reason why they bent underneath the cells, thus, it is still an unanswered question whether the same pillar geometry and dimensions would induce the same biological response if there is no tip displacement and bending. Moreover, these pillars were fabricated on a very small area (1 mm^2) which limits practicing certain biological assays. In this study, to show the potential of the fabrication process developed in this study, we used EBL to pattern a large area (3 $\times$ 5 mm^2) of fused silica substrates (significantly stiffer than the polymeric resin used in two-photon polymerization) with submicron pillars whose dimensions were similar to those of the abovementioned study. The EBL parameters, including resist type, resist thickness, exposure parameters (*e.g.,* beam current, spot size, and electron dosage), and mask thickness were optimized to generate submicron pillars with the highly precise dimensions in as short of a processing time as possible. We then, for the first time, cultured preosteoblasts on a fused silica substrate containing submicron pillars that were made of the same material to study the interaction of the preosteoblasts with the submicron features of fused silica and verify that the effects of the submicron pillars on those cells are independent from the chemical properties and stiffness of the material. Moreover, we created hybrid PDMS molds (replica of the master mold) that enabled us to replicate the patterns multiple times, thereby substantially decreasing the costs and time associated with the proposed nanofabrication process and making it possible to economically produce large enough number of specimens. Fused silica was chosen as the final substrate and by finding the appropriate hard mask, thermoplastic resist, etching gasses, and nanoimprint parameters, the desired submicron patterns were successfully replicated from the hybrid PDMS replica mold into the fused silica substrate. The high transparency and mechanical properties of fused silica make it a proper candidate for both UV and thermal NIL. Although there are some studies on transferring the nano/submicron features into the different types of polymers using NIL technique, to the best of our knowledge, there is no study on transferring them onto fused silica which has more relevant properties for the intended research and clinical applications.

2. Materials and methods

2.1. Master mold fabrication by EBL

The process steps involved in the fabrication of the master mold are illustrated in Fig. 1a. Double side polished 4-inch (diameter = 10.16 cm) fused silica wafer (thickness = 525 $\pm$ 25 µm) (University Wafers Inc, MA, USA) was cleaned in the Piranha solution (a mixture of 3:1 (v/v) H_2SO_4 (Honeywell, Bucharest, Romania) and H_2O_2 (VWR international, Amsterdam, The Netherlands)) at room temperature for 12 min, was rinsed with deionized (DI) water, and was dried with a nitrogen gun. The wafer was then covered with a thin layer of photoresist to protect its surface from damage. Subsequently, the wafer was diced into 1 $\times$ 1 cm^2 specimens using a disco dicer (Disco Hi-Tec Europe GMbH, Munich, Germany). After dicing, the photoresist layer was removed by placing the pieces into acetone (Sigma-Aldrich, The Netherlands) combined with ultrasonication for 20 min. The cleaning process was followed by immersing the specimens in isopropyl alcohol (IPA, Sigma-Aldrich, The Netherlands) and DI water, respectively, and drying them with a nitrogen gun.

Polymethyl methacrylate (PMMA) resist (495, A8) (495 K molecular weight, 8 wt% in anisole, Microchem Corp, USA) was spun coat on the fused silica substrate at 3000 rpm and was baked at 185 °C on a hotplate for 20 min. Once it cooled down, PMMA AR-P 679.02 (950 K, ALLRESIST GmbH, Germany) was spun coat on the specimen at 6000 rpm. The specimen was then baked at 185 °C for 10 min. A multilayer resist was used to make the lift-off process easier. The resist thickness was measured using a Dektak profilometer (Bruker, Karlsruhe, Germany). Then, 15 nm of chromium (Cr) with a rate of 0.5 °A/sec was evaporated on the specimens using an e-beam evaporator (Temescal FC-2000, Ferrotec, Germany) to make them conductive before e-beam exposure. The PMMA resist was directly patterned using EBL (Raith EBPG 5200) operated at an acceleration voltage of 100 kV and a beam current of 364 pA. The designed file included circular features with a diameter of 250 nm and two different values of interspacing, namely 700 nm and 1000 nm. As the optimized electron dosage had to be

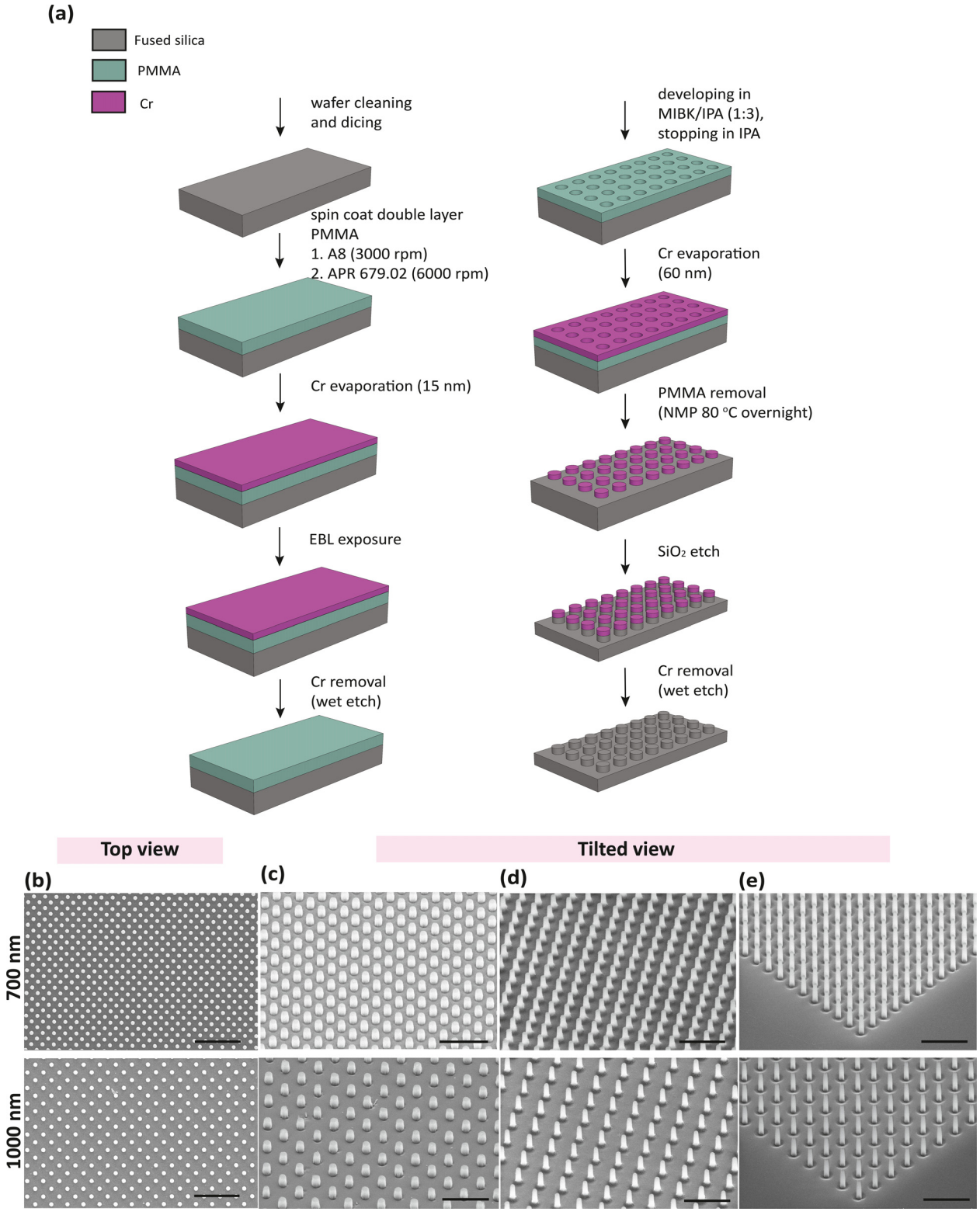

Fig. 1. (a) A schematic drawing of the procedure of fabricating submicron pillars on the fused silica master mold using electron beam lithography. Top (b) and tilted (c-e) SEM images of the resulting submicron pillars with the interspacing values of 700 and 1000 nm formed on the fused silica substrate. Scale bar = 2 μm. (c) submicron pillars after 255 s of etching using ICP RIE, (d) submicron pillars after 8 min of etching using ICP RIE, and (e) submicron pillars after 90 min of etching using RIE.

determined for each dimension, a broad range dose test was performed from 500 $\mu C/cm^2$ to 2000 $\mu C/cm^2$. After exposure, the Cr layer was removed by immersing the specimens in a Cr etchant (Chromium Etchant N1, MicroChemicals, Ulm, Germany) for 20 sec. The specimens were then rinsed in DI water for 5 min and were dried with a nitrogen gun. The PMMA resist was developed using a methyl isobutyl ketone (MIBK, Sigma-Aldrich, The Netherlands)/IPA 1:3 solution for 75 sec, rinsing in IPA for 30 sec, and drying with a nitrogen gun. To remove the resist residues from the holes, the specimens were exposed to an oxygen plasma (PVA

Tepla M4L Gas Plasma System, Corona, USA) with an oxygen gas flow rate of 200 sccm and a power of 100 W for 20 sec. After the plasma treatment, 60 nm Cr was deposited on the specimen as a mask using an e-beam evaporator (evaporation rate = 0.5 °A/sec, chamber pressure = 1.5×10^{-6} mbar). A lift-off process was performed to remove the resist from the area around the features. To do so, N-Methyl-2-pyrrolidone (NMP, Sigma-Aldrich, The Netherlands) was heated up to 80 °C and was used for soaking the specimens for 2 hours. To transfer the patterns into the substrate and create the submicron pillars, two different etching methods of the fused silica were investigated: ICP RIE (Adixen AMS 100 I-speeder, Alcatel, France) or RIE (Sentech Etchlab 200, Sentech Instruments, Germany). In the case of ICP RIE, a gas mixture of $C_4F_8/CH_4/He$ (15/15/150 sccm) was used for different durations to reach the desired height. The other etching parameters were as follows: a source power of 2500 W, a bias voltage of 23 V, and a temperature of 0 °C. In the case of RIE, a gas mixture of CHF_3/O_2 (68/5 sccm) with an RF power of 102 W, a bias voltage of 340 V, and a chamber pressure of 15 µbar were used. As the submicron pillars were formed on the fused silica substrate, the Cr mask was removed by immersing the specimens into the Cr etchant for 20 sec. This process was followed by rinsing the specimen with DI water for 5 min. The final step before SEM inspection was cleaning the specimens with the piranha solution for 12 min to remove the organic and polymeric contaminants which had formed on the substrate during the etching process, followed by rinsing with DI water for 5 min and drying with a nitrogen gun.

Top and tilted SEM images of the resultant master mold were taken using a Helios Nano Lab 650 (FEI company, US) SEM, with an acceleration voltage of 10 kV and a beam current of 50 pA. The diameter and height of the submicron pillars were measured from the tilted SEM images, while the interspacing values were measured from the top view SEM images.

2.2. Interactions of MC3T3-E1 preosteoblast cells with the patterned surfaces

All the fused silica specimens were sterilized prior to cell seeding by immersing them in 70% ethanol and exposing them to UV light for 20 min. The specimens were rinsed twice with 10X phosphate buffered saline (PBS, Sigma-Aldrich, Germany), were submerged in a solution of 50 μg/ml bovine fibronectin (Sigma-Aldrich, US), and were incubated at 37 °C and 5% CO_2 for 30 min to improve the cell adhesion [48]. MC3T3-E1 preosteoblast cells (Sigma-Aldrich, Germany) cultured in the alpha minimum essential medium (α-MEM) supplemented with 10% (v/v) fetal bovine serum (FBS) and 1% (v/v) penicillin-streptomycin (all from Thermo Fisher Scientific, US) were seeded on the specimens (1×10^4 cells per sample) in a 24 well-plate (Greiner, Bio-One, The Netherlands) and were incubated at 37 °C and 5% CO_2.

After 1 day of culture, the specimens (n=3) were washed twice with 10X PBS and the cells were fixated using a 4% (v/v) formaldehyde solution (Sigma-Aldrich, Germany). Following the cell membrane permeabilization using 0.5% Triton X-100/PBS (Sigma-Aldrich, Germany) at 4 °C for 5 min, the samples were incubated in 1% BSA/PBS (Sigma-Aldrich, Germany) at 37 °C for 5 min. The specimens were then incubated in anti-vinculin mouse monoclonal primary antibody (1:100 in 1% BSA/PBS, Sigma-Aldrich, Germany) and rhodamine-conjugated phalloidin (1:1000 in 1% BSA/PBS, Thermo Fisher Scientific, US) for 1 h at 37 °C. The cells were then washed three times with 0.5% Tween-20/PBS (Sigma-Aldrich, Germany) and were incubated in Alexa Fluor 488 (*i.e.*, donkey anti-mouse polyclonal secondary antibody, 1:200 in 1% BSA/PBS, Thermo Fisher Scientific, US) for 1 h at room temperature. After washing with 0.5% Tween-20/PBS and 1X PBS, the samples were mounted on microscopic glass slides using 10 µl of the Prolong gold antifade reagent containing DAPI (4',6-diamidino-2-phenylindole) (Thermo Fisher Scientific, US). Finally, the specimens were imaged using a fluorescence microscope (ZOE™ fluorescent cell imager, Bio-Rad, The Netherlands). For the SEM observations, the stained samples (n=3) were washed twice with distilled water for 5 min and were then dehydrated in 50%, 70%, and 96% ethanol solutions for 15 min, 20 min, and 20 min, respectively. After air-drying overnight at room temperature, the samples were gold-sputtered before SEM imaging.

To evaluate the osteogenic properties of the patterned surfaces, the cells were stained for osteopontin (OPN) after 21 days of culture in osteogenic medium. Following the fixation and permeabilization of cells, they were incubated with OPN antibody conjugated to Alexa fluor 488 (1:100 in BSA/PBS, Santa Cruz Biotechnology, US) for 1 h at 37 °C (n=3).

ImageJ 1.53c (NIH, US) was used to quantify the morphological characteristics of the cells as well as the area of focal adhesions and OPN according to methods described before [49,58].

2.3. Contact angle measurements

A drop shape analyzer (KRUSS DSA100, Germany) was used to evaluate the wettability of the surfaces used for cell culture (*i.e.*, the flat and patterned surfaces, n=3). A droplet of deionized water with a volume of 3.0 μL was placed on the surface. The images were recorded after 5 sec.

2.4. Fabrication of the hybrid PDMS replica molds

A schematic drawing illustrating the process steps of soft lithography is presented in Fig. 2a. Prior to performing hybrid PDMS molding, the fused silica master mold was first placed, for 30 min, in a vacuum desiccator close enough to a glass petri dish containing a droplet of octyltrichlorosilane (OTS) (Gelest Inc., Germany) to coat the surface of the master mold with a hydrophobic layer, thereby preventing the cured hybrid PDMS layer from sticking to the master mold. The hybrid PDMS mold consisted of two layers: a thin layer of hard-PDMS (hPDMS) (a 30-40 µm stiff layer), that was in direct contact with the patterns during the molding process, and a PDMS (a 3-5 mm flexible layer) that formed the bulk of the replica mold. The hPDMS was made by mixing 0.85 g of 7-8 % (vinylmethylsiloxane)-dimethylsiloxane copolymer, trimethylsiloxy terminated (Gelest Inc., Germany), 2.0 µl of 2,4,6,8-Tetramethyl-2,4,6,8-tetravinylcyclotetrasiloxane (Sigma Aldrich, Germany), and 3.0 µl of platinum-divinyltetramethyldisiloxane complex in xylene (Gelest Inc., Germany) for 5 min. This combination was left in a vacuum desiccator for 30 min to remove the air bubbles present in the mixture. After this step, 0.25 g of (25-35 % methylhydrosiloxane)-dimethylsiloxane (PDMS copolymer, 25-35 cSt, Gelest Inc, Germany) was added to the previous mixture, was mixed for 3 min, was poured, and was spun coat on the fused silica master mold for 40 sec using a spinning rate of 1000 rpm, followed by curing in an oven at 60 °C for 20 min. PDMS (Sylgard 184, Dow Inc., Midland, MI, U.S.A.) combined with the curing agent at a weight ratio of 10:1 was mixed thoroughly, cast on the master mold, and desiccated in vacuum for 30 minutes to remove the air bubbles. The fused silica master mold (with the hybrid PDMS on top) was then cured in an oven at 40 °C for 16 h. After curing, the hybrid PDMS was carefully peeled off from the substrate. The master and the replica molds were finally sterilized by IPA. We verified that the same master mold could be used at least 5 times to apply the patterns into PDMS without a significant loss of fidelity.

The quality of the patterns replicated into the hybrid PDMS was evaluated using SEM. Prior to SEM imaging, the PDMS substrates were gold-sputtered.

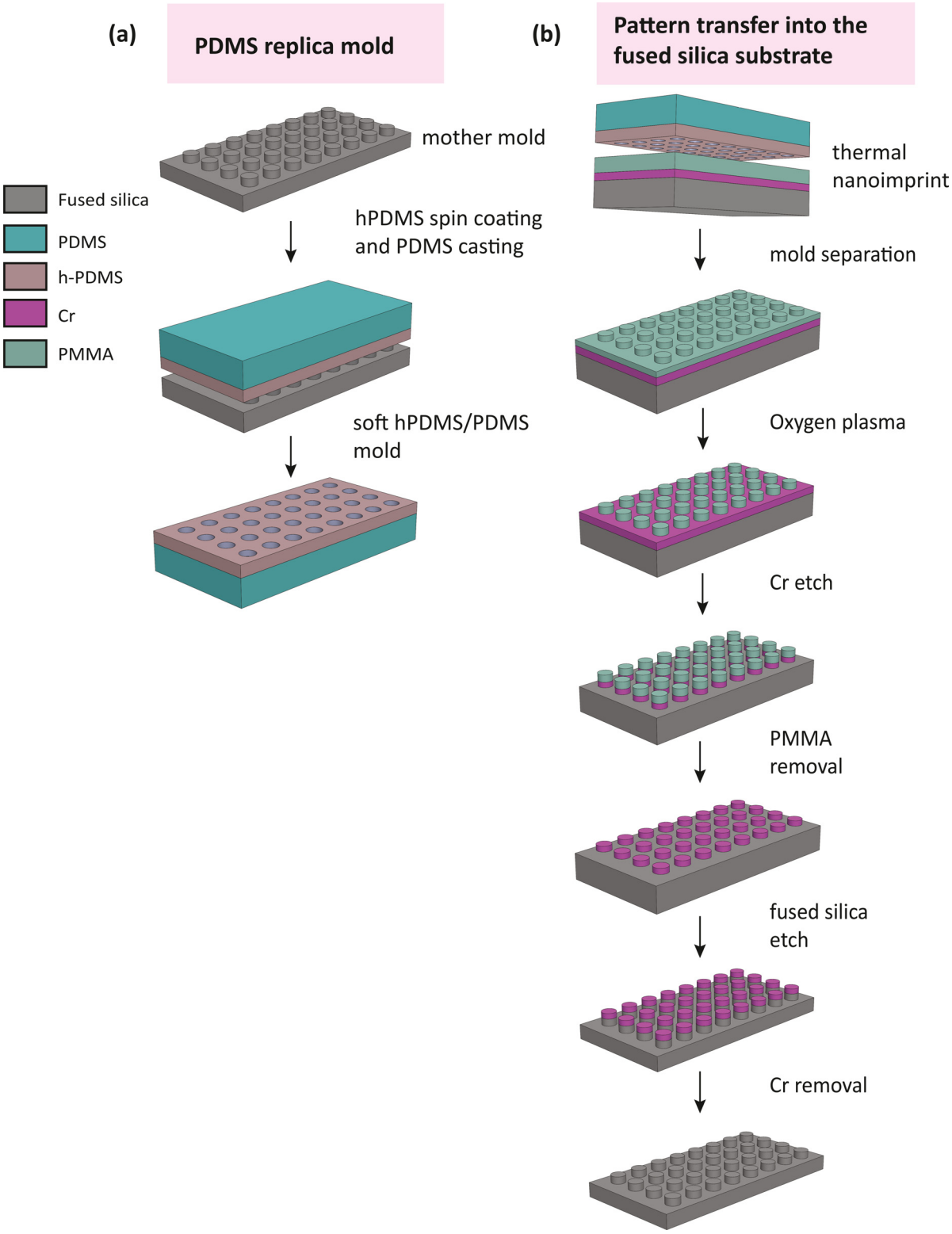

Fig. 2. A schematic drawing of (a) the steps involved in the preparation of the hPDMS/PDMS daughter molds and (b) the thermal nanoimprint process used to transfer the submicron pits from the hPDMS/PDMS mold to the fused silica substrate.

2.5. Cross-sectional characterization using FIB milling

In order to measure the depth of the replicated patterns (submicron pits) on the hybrid PDMS mold, focused ion beam scanning electron microscopy (FIB-SEM) was performed in a FIB microscope (FEI, Helios G4 CX dual beam workstation, Hillsborough, USA). The specimen was tilted to 52° and the surface was milled using Gallium ions with a 7 pA ion beam (acceleration voltage = 30 kV).

2.6. Pattern transfer from the hybrid PDMS replica mold to the substrate of interest by thermal nanoimprint

The details of the process steps involved in NIL are presented in Fig. 2b.

Firstly, Cr (30 nm) was evaporated on the 1 × 1 cm^2 fused silica specimens. PMMA (950 A3) (950 K molecular weight, 3 wt% in anisole, Microchem Corp, USA) was then spun coated on the specimens at 4250 rpm, and baked on a hotplate at 185 °C for 20 min. The nanoimprinting was carried out using a commercial thermal nanoimprinting EVG bonder (EVG 520, EVgroup, Austria). The hybrid PDMS replica mold containing submicron pits and the fused silica specimens were brought into contact with each other (hybrid PDMS on top and fused silica at the bottom). The temperature was then increased to above the glass transition temperature (T_g) of PMMA (140 °C) (T_g of PMMA = 105 °C). The hybrid PDMS mold was then pressed into the PMMA layer with a set force of 1250 N for 3 min at the embossing temperature. After imprinting, the chamber was cooled down below T_g (80 °C in this study) with a rate of 2 °C/min. The slow cooling rate was chosen to reduce the thermal stress caused by cooling in the material. To prevent the polymeric microstructures from flattening and rounding of the edges, the embossing force was maintained during the cooling down process. The force was released one minute after reaching 80 °C (de-embossing temperature). The cooling down process was continued to reach 40 °C, and then the hybrid PDMS mold and the fused silica specimen were separated gently and taken out from the chamber afterward.

To transfer the submicron pillars formed on the PMMA into the fused silica substrate underneath, we first used oxygen plasma to remove the residues of the PMMA that rest in between the pillars (Fig. 2b) in a process called *descum*. The descum process was performed using 20 sccm O_2 plasma, with a power of 20 W, and at a chamber pressure of 40 μbar in a plasma etcher- RIE Etchlab 200 (Sentech Instruments, Germany) for 2 min.

To have access to the surface of the fused silica specimens, the Cr layer was etched using a Chlorine-based ICP RIE machine (PlasmaLab System 100, Oxford Instruments, UK) while employing PMMA as the mask. The etching process was conducted under the following conditions: RF power = 50 W, Cl_2 = 50 sccm, O_2 = 5 sccm, temperature = 40 °C, chamber pressure = 12.5 μbar, and etching time = 90 sec. Once the patterns were transferred into the Cr layer, the PMMA mask could be removed. To do so, the specimens were soaked in NMP at 80 °C overnight. This step was followed by transferring the submicron pillars into the fused silica substrate, by using the Cr layer as the mask during the etching step. The fused silica was etched using ICP RIE (Adixen AMS100 I-speeder, Alcatel, France), by C_4F_8/CH_4/He: 15/15/150 sccm as the etching gasses for 4 min and 15 sec, and with a source power of 2500 W, an RF power of 250 W, a bias voltage of 23 V, and at 0 °C. The Cr mask was then etched away using the Cr etchant and the specimens were dried using a nitrogen-gun and were gold-sputtered before SEM imaging.

2.7. Statistical analysis

To statistically analyze the results of cell culture experiments, the raw data was first tested for normal distribution using the D'Agostino-Pearson omnibus normality test in Prism version 9.1.2 (GraphPad, US). For normally distributed datasets, the Brown–Forsythe and Welch ANOVA test was performed, followed by the Dunnett's T3 multiple comparisons test to determine the statistical significance of the differences between the means of the different experimental groups. For the datasets which did not pass the normality test, the non-parametrical Kruskal–Wallis test was performed, followed by the Dunn's multiple comparisons test. All data are presented as mean ± standard deviation and a *p*-value below 0.05 was considered to indicate statistical significance.

3. Results

3.1. Fabrication and characterization of the master mold

In the case of ICP RIE and after 255 s of etching, the submicron pillars with an interspacing of 700 nm had a height of 508 ± 24 nm and a diameter of 269 ± 19 nm while the submicron pillars with an interspacing of 1000 nm had a height of 523 ± 25 nm and a diameter of 275 ± 22 nm (Fig. 1c). After 8 min of ICP RIE etching, the submicron pillars with an interspacing of 700 nm had a height of 990 ± 37 nm and a diameter of 245 ± 22 nm while the submicron pillars with an interspacing of 1000 nm had a height of 1046 ± 31 nm and a diameter of 255 ± 31 nm (Fig. 1d). In the case of RIE, after 90 min of etching, a height of 973 ± 43 nm and a diameter of 206 ± 14 nm was reached for the submicron pillars with an interspacing of 700 nm while the submicron pillars with an interspacing of 1000 nm had a height of 1068 ± 41 nm and a diameter of 222 ± 13 nm (Fig. 1e).

3.2. Adaptation of preosteoblasts to the patterned surfaces

MC3T3-E1 preosteoblast cells presented different morphologies on the flat and patterned surfaces (the ones etched using ICP RIE for 8 min) after 1 day of culture (Fig. 3a-c and Fig. S1). While the majority of the cells had a polygonal shape on the flat surfaces, more cells with a stellate or polarized shape [6] could be recognized on the patterned surfaces (Fig. 3a). The actin fibers in most of the cells residing on the flat areas were oriented towards the vertices of the polygonal shape of the cell body (Fig. 3b). Interestingly, actin fibers were collectively organized more homogenously along the whole cell body in the polarized cells residing on the submicron pillars with an interspacing of 700 nm. Nevertheless, the cytoskeleton was less organized in the cells cultured on the submicron pillars with an interspacing of 1000 nm as compared to the last two surfaces. Further SEM observations revealed different settling states for the cells residing on submicron pillars with different values of interspacing. A "top state" was identified for the cells residing on the submicron pillars with an interspacing of 700 nm, meaning that the cell body was on top of the pillars (Fig. 3c, d and Fig. S2). The cells on the submicron pillars with an interspacing of 1000 nm, however, presented a "mixed state" in which the areas of the cell closer to the cell nucleus seemed to be in a "top state" while farther from these regions (*i.e.,* at the cell periphery), showed a "bottom state". At these regions, the cell was not only in contact with both the tip and lateral sides of the pillars but also with the substrate.

The cell projected area decreased as the interspacing of the submicron pillars increased (Fig. 4a). An opposite trend was observed for the cell aspect ratio (*i.e.,* more polarization for the larger interspacing value). However, the cell shape index (*i.e.,* the roundness of the cells) was not significantly different between the flat and patterned surfaces. Despite the differences in the cell nucleus projected area and shape index between the flat controls and the patterned surfaces with an interspacing of 700 nm, a discernible trend was not observed regarding the effects of interspacing on the morphological characteristics of the nucleus (Fig. 4b).

The average FA area was found to be significantly affected by the surface topography. The cells residing on the submicron pillars with an interspacing of 700 nm formed significantly smaller FAs as compared to the flat controls and patterned surfaces with an interspacing of 1000 nm (Fig. 4c). Finally, the expression of OPN in the matrix was significantly upregulated on the patterned surfaces (Figs. 3c and 4d). The pillars with an interspacing of 1000 nm were

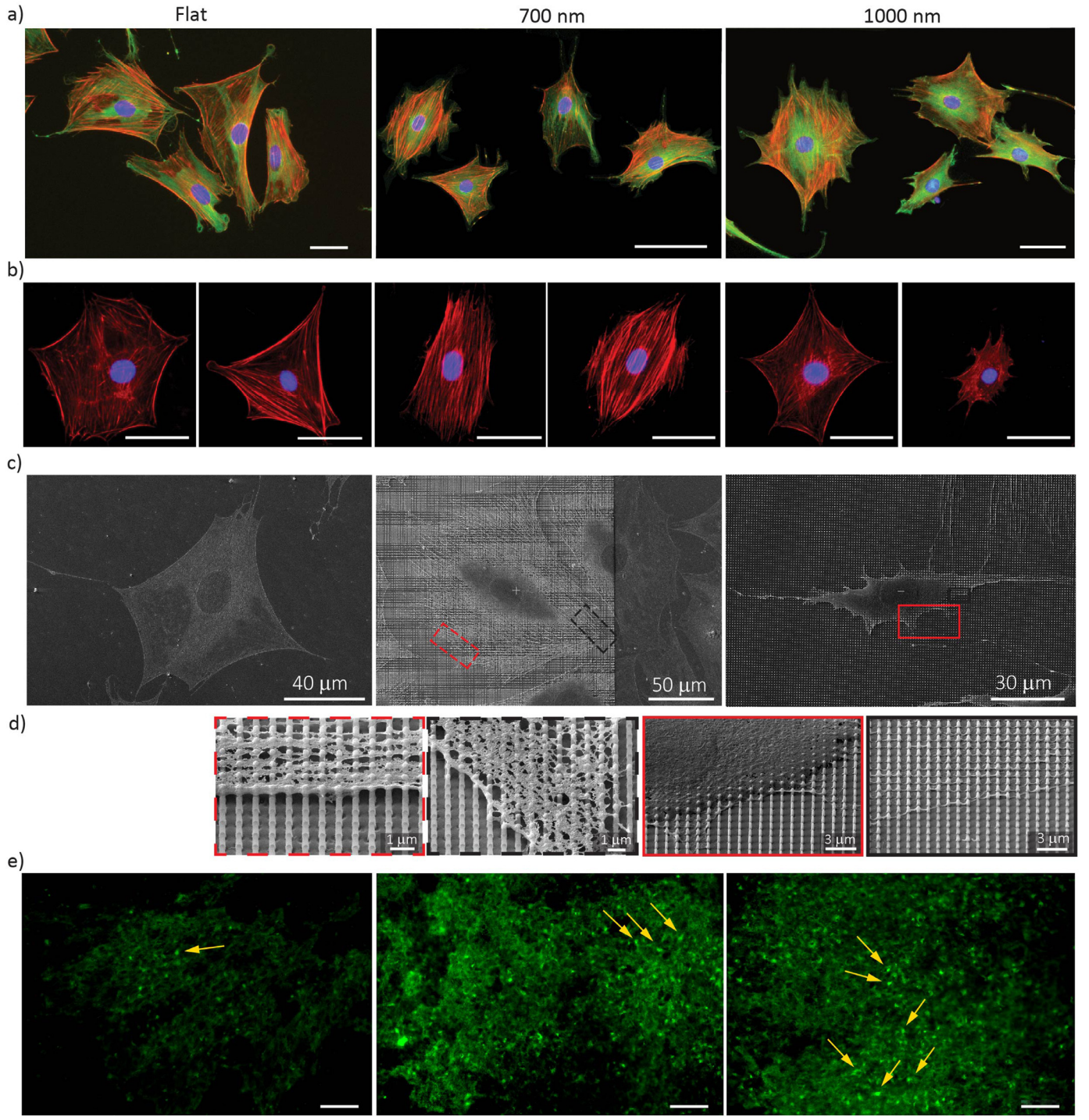

Fig. 3. (a) Immunofluorescent staining of vinculin (green), actin (red), and nucleus (blue) of the MC3T3-E1 preosteoblast cells cultured on the flat and patterned specimens for 1 day. Scale bar = 100 µm. (b) Representative images of the cytoskeletal organization of the cells residing on the flat and patterned specimens (red: actin and blue: nucleus). Scale bar = 20 µm. (c) Top view SEM images of the representative cell morphology on the flat and patterned specimens. (d) Highly magnified tilted SEM views of the settlement state of the cells on the patterned specimens and their interactions with the single pillars at cell periphery. (e) The expression of OPN visualized using immunostaining after 21 days.

found to have a significantly higher potential for promoting OPN expression as compared to the pillars with an interspacing of 700 nm.

3.3. Water contact angle

While the contact angle for the flat fused silica was 34.0 ± 3.3° (n = 3), it was significantly decreased to 7.0 ± 4.3° (n = 3) on the patterned fused silica specimens with an interspacing of 700 nm and to 9.0 ± 6.3° (n = 3) on the patterned fused silica specimens with an interspacing of 1000 nm, indicating the super-hydrophilicity of the patterned surfaces (Fig. 4e).

3.4. Fabrication and characterization of the replica mold

The hybrid PDMS mold, containing two sets of submicron pit arrays were successfully replicated from the fused silica master mold with the shorter submicron pillars (the one illustrated in

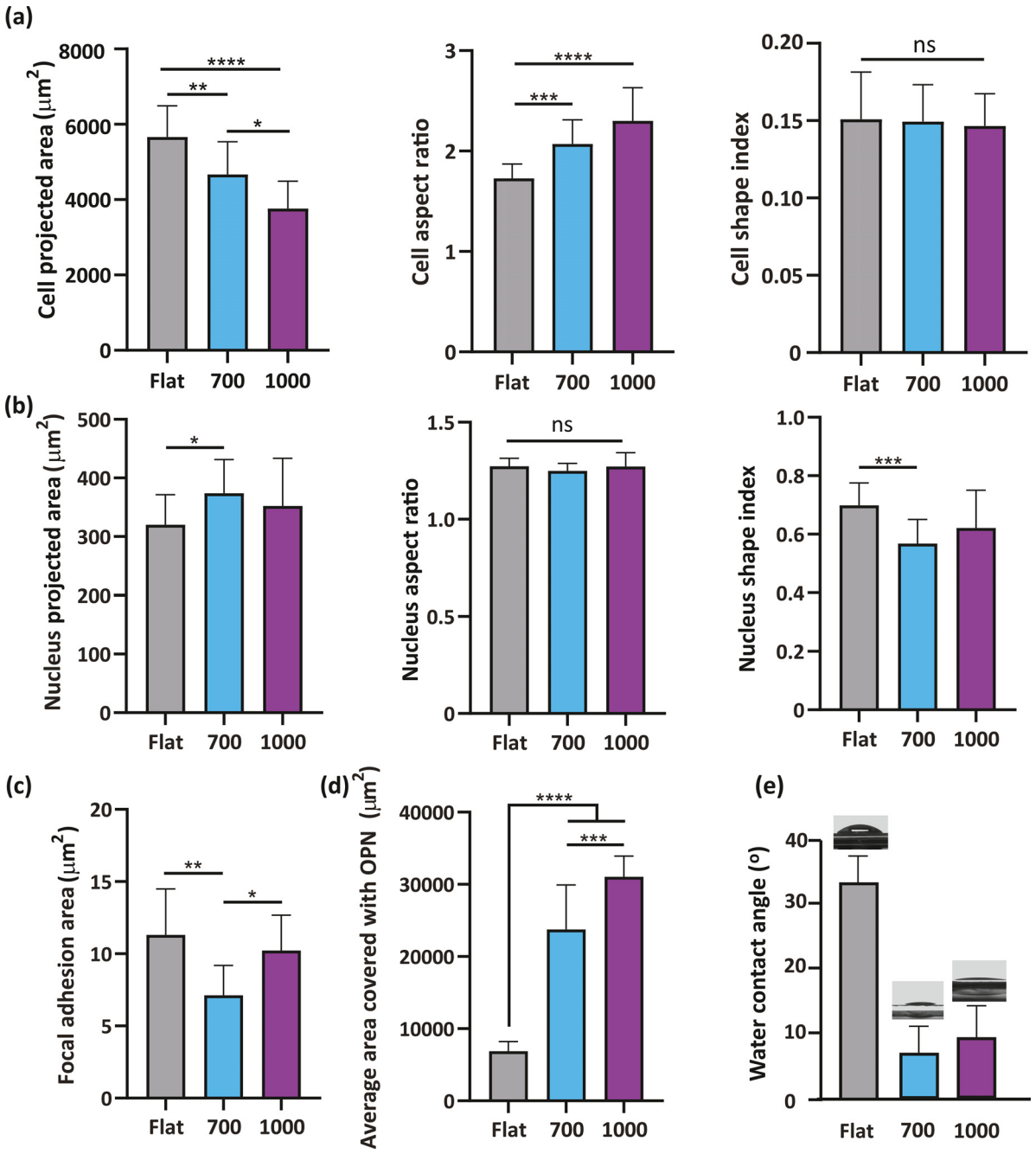

Fig. 4. (a) The morphological characteristics of the preosteoblasts *(i.e.,* projected area, aspect ratio, and shape index) cultured on the flat (n=3) and patterned (n=3) specimens after 1 day. (b) The morphological characteristics of the cell nucleus *(i.e.,* projected area, aspect ratio, and shape index) cultured on the flat (n=3) and patterned (n=3) specimens after 1 day. At least 250 cells were analyzed for each geometrical parameter. (c) The average focal adhesion area of the cells residing on the flat (n=3) and patterned (n=3) specimens. At least 10 cells were analyzed per study group. (d) The average area covered with OPN after 21 days (n=3). At least 8 images were taken from each sample of each study group for quantification of OPN area. (e) Water contact angle on the flat (n=3) and patterned (n=3) specimens. (* $p < 0.05$, ** $p < 0.01$, *** $p < 0.001$, and **** $p < 0.0001$).

Fig. 1c and Table 1). The patterns replicated into the PDMS were geometrically similar to the original patterns (Fig. 5a). SEM images indicated no irregularity, clogging, or any other artifacts or signs of incomplete replication of the submicron pits or any damaging of the imprinted substrate (Fig. 5a, b). The average diameter and interspacing of the replicated submicron pits, measured on SEM images, confirm the precision of the imprinted patterns (Table 1). To quantify the submicron pits, FIB milling of the submicron pits was performed. The depths measured were 428 ± 55 nm and 402 ± 25 nm for the submicron pits with the interspacing values of 700 nm and 1000 nm, respectively (Fig. 5c).

The SEM images of the fused silica master mold, after gently peeling off the hybrid PDMS from it, revealed that the morphology of the submicron pillars had not changed and that there were no significant differences between the dimension of the submicron pillars before PDMS molding and after it (Fig. 5d and Table 1). Furthermore, only negligible amounts of PDMS residues remained in-between the submicron pillars, confirming that the fused silica master mold can be used for several rounds of molding without being damaged.

Table 1
The means and standard deviations of the dimensions of the submicron patterns produced/replicated after the application of every fabrication technique.

		design interspacing = 700 nm				design interspacing = 1000 nm			
mold	pattern type	diameter (nm)	interspacing (nm)	height (nm)	aspect ratio	diameter (nm)	interspacing (nm)	height (nm)	aspect ratio
master mold (fused silica) before molding	submicron pillars	269 ± 19	712 ± 13	509 ± 25	1.9 ± 0.2	275 ± 22	1013 ± 21	523 ± 25	1.9 ± 0.2
replica mold (hybrid PDMS)	submicron pits	293 ± 20	685 ± 24	–	–	245 ± 28	980 ± 33	–	–
master mold (fused silica) after molding	submicron pillars	275 ± 19	702 ± 14	516 ± 20	1.9 ± 0.2	291 ± 16	1003 ± 15	517 ± 25	1.7 ± 0.1
final patterns (fused silica)	submicron pillars	235 ± 19	720 ± 12	501 ± 27	2.1 ± 0.2	221 ± 13	1022 ± 18	492 ± 30	2.2 ± 0.2

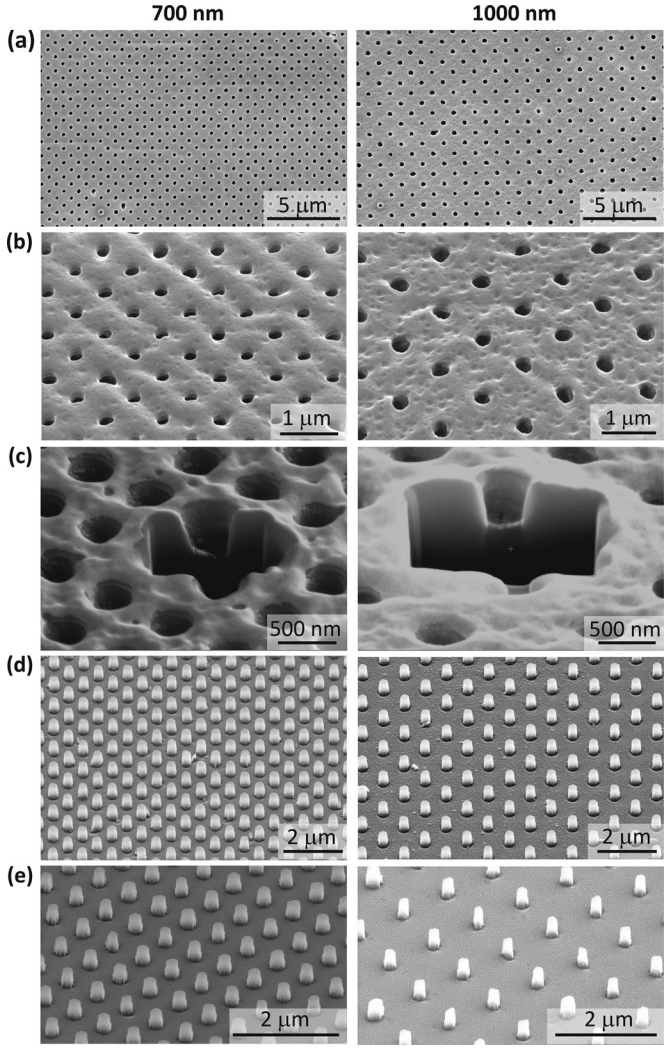

Fig. 5. (a) Top and (b) tilted SEM images of the replica patterns (*i.e.,* submicron pits) that were successfully transferred into the hybrid PDMS mold. (c) SEM image of the hybrid PDMS replica mold after FIB milling showing the depth of the submicron pits. (d) SEM images of submicron pillars present on the master mold after peeling off the PDMS that confirm the patterns were nicely transferred into the PDMS without damaging or destroying the master mold. (e) SEM images of the successfully transferred submicron pillars into the fused silica substrate.

3.5. Characterization of the patterns transferred into the fused silica substrate through thermal nanoimprinting

The heights of the transferred submicron pillars with the interspacing values of 700 nm and 1000 nm, after 255 sec etching of fused silica using Cr mask, were respectively 501 ± 27 nm and 492 ± 30 nm (Table 1, Fig. 5e).

4. Discussion

The design and fabrication of bioinspired and/or rationally designed nanoscale and submicron patterns on the surface of biomaterials could enhance their functionality by eliciting certain cell responses and guiding cells towards the desired lineages. The development of high-throughput and highly precise fabrication processes that make it feasible to fabricate large areas of patterned surfaces on a variety of substrates regardless of their composition and geometry (*i.e.,* flat or curved) is of importance. The main challenge here lies in simultaneously achieving high geometrical precision and high throughput. There has hardly been any nanofabrication technique that can satisfy both requirements. For instance, such techniques as ICP RIE and hydrothermal treatment enable the rapid production of nano/submicron patterns over a large area but are limited in their geometrical precision when compared with low-throughput techniques, such as EBID, EBL, or FIB, while also not being able to adjust every single design parameter independent from the others [21,22]. The main contribution of this study, therefore, is the development of a rapid and accurate fabrication process to overcome the abovementioned challenges. Nanoimprint lithography offers geometrical precision and high resolutions on the one hand and high-throughput on the other. Moreover, it provides the opportunity to transfer the patterns into the flat and curved substrates as well [50–52]. The availability of such techniques is expected to enable more extensive studies of the interactions between cells and nanopatterns, thereby broadening our knowledge of how cells interact with surface topography and how topographical cues can be exploited to promote tissue regeneration. While other materials, such as titanium alloys, may be more suitable as bone substitutes, we used fused silica in the current study to benefit from its high transparency that makes it an ideal material for both thermal and UV nanoimprint lithography, as well as for imaging purposes during cell studies.

4.1. Interactions of MC3T3-E1 cells with patterns

The early-stage adaptation of the cells to the surface and their interactions with the topographical cues of the surface largely determine the long-term response of cells, including their osteogenic differentiation [6]. It has been shown that cell shape and area affect the cytoskeletal organization, as well as the formation and distribution of FAs, which together modulate the stem cells fate [53–55]. Cell shape can also regulate the phenotype independently from tension-based mechanisms [56]. Moreover, in the case of high aspect ratio pillars, direct nuclear mechanotransduction pathways could determine the cell fate [57]. In our study, the submicron pillars significantly affected the morphological characteristics of the

cells in terms of area and aspect ratio. In agreement with a number of reports available in the literature, the presence of the pillars on the biomaterial surface decreased the cell spreading area [58–60]. The spreading area decreased further as the pillar interspacing increased [58–60]. It seems that as the pillars become more separated, the cells tend to confine their area to secure their initial adhesion points as well as an optimized membrane trafficking [61,62]. The differences in the cytoskeletal organization and FA area between the 700 nm and 1000 nm submicron pillars could be interpreted within this context. The cells residing on the 1000 nm submicron pillars likely undergo a slower adaptation as their actin fibers are not yet well-oriented (as compared to the cells residing on the 700 nm submicron pillars). On the other hand, a larger FAs area on the 1000 nm submicron pillars may be indicative of the fact that the cells are still attempting to form stronger adhesions to the surface.

The increased cell aspect ratio (*i.e.,* elongation) is believed to be beneficial for osteogenic differentiation [18,63]. The increase in the cell aspect ratio has been shown to increase the anisotropy of FAs [53,64]. Similarly, we observed that the FAs are preferentially formed at the periphery of smaller and more elongated cells, especially on the 1000 nm submicron pillars. The increased expression of OPN on the 1000 nm pillars suggests that the elongation of the cells and the differential distribution of FAs at the early stages of adaptation to the surface may favorably promote osteogenic differentiation.

Different settling states in the cells residing on the submicron pillars with different interspacing values could be another factor and/or indicator of the varied cytoskeletal organization. The “top state” observed on the submicron pillars with an interspacing of 700 nm ensures that the cells maintain a global convex geometry (from the cell periphery towards the nucleus), which is shown to be associated with higher forces exerted on the nucleus and eventually lead to higher levels of osteogenic differentiation [65]. The “mixed state” observed on the submicron pillars with an interspacing of 1000 nm, on the other hand, imposes a different geometry on the cells at some regions as there is a significant difference in the height between the nuclear area (the thickest part of the cell body) and the cell periphery (deeply sunk into the submicron pillars). This might hinder or delay the global cytoskeletal organization. In a previous study involving pillars with the same dimensions made of a commercial polymer, the pillars with an interspacing of 700 nm, which induced a “top state” to the cells, showed the highest expression of OPN [6]. Since the pillars in that study were bent underneath the cells, the traction forces were, therefore, assumed to have been transferred all the way to the nucleus via a direct mechanotransduction pathway, affecting the long-term osteogenic response of the cells. In the present study, however, the pillars were stiff enough to not be bent. There may, therefore, be some differences in the cell traction forces observed in these two studies.

In the current study, the pillars inducing the “mixed state” maximized the expression of OPN. It could, therefore, be postulated that engulfing the high aspect ratio pillars by cells in a “mixed state” of the settlement could also trigger direct or indirect mechanotransduction pathways that eventually increase the expression of osteogenic markers, such as OPN [66]. Given that a higher substrate stiffness and a reduced cell area lead to the exertion of larger traction forces [59], further studies using traction force microscopy might shed some light on the origins of the observed differences in the OPN expression between the pillars with different interspacing values. Nevertheless, the results of this study show that submicron pillars with specific geometry and dimensions have a significant effect on the osteogenic differentiation of cells regardless of their material. Therefore, having the possibility to produce such submicron pillars using high-throughput methods that enable generation of a large number of samples with acceptable reproducibility on various substrates is essential for further research.

4.2. Water contact angle

The super-hydrophilicity of the patterned surfaces is in good agreement with the predictions of Wenzel model [67,68]. In this model, it is assumed that the liquid penetrates in between the pillars. The contact angle of a rough surface (θ_w) can then be estimated using the following equation:

$$cos(\theta_w) = \quad r\,cos(\theta) \tag{1}$$

where θ_w and θ are respectively the contact angles of the droplet on the patterned and flat substrates and r is the ratio of the real surface area to the projected surface area, called the roughness factor. Assuming the pillars to be cylindrical in shape with a diameter of d, a height of h, and a pitch of p, r can be calculated as [26]:

$$r = \frac{A_{real}}{A_{projected}} = \frac{p^2 + 4\left(\frac{\pi dh}{4}\right)}{p^2} = 1 + \frac{\pi dh}{p^2} \tag{2}$$

Based on the Wenzel relation Eq. (1)), a hydrophilic surface ($\theta < 90°$) becomes more hydrophilic after patterning ($\theta_w < \theta$)[68]. Substituting the dimensions of the submicron pillars ($d = 245$ nm, $h = 990$ nm for $p = 700$ nm and $d = 255$ nm, $h = 1046$ nm for $p = 1000$ nm) and $\theta = 34°$ into Eqs. (1) and ((2) yields $r = 2.14$ and $cos(\theta_w) > 1$ for $p = 700$ nm, and $r = 1.54$ and $cos(\theta_w) > 1$ for $p = 1000$ nm. $cos(\theta_w) > 1$ in both cases indicates that the surface becomes completely wet (*i.e.*, the surface is super-hydrophilic), which is in a good agreement with the results of our experiments, where the measured contact angle was $7 \pm 4°$ and $9 \pm 6°$ for $p = 700$ nm and $p = 1000$ nm, respectively (Fig. 4e).

4.3. Hybrid PDMS molding

The PDMS molds suffer from some limitations. First, due to the low elastic modulus of PDMS, patterns with very high or very low aspect ratio deform, collapse, or buckle and create some defects on the patterned areas during the molding process, meaning that the patterns cannot be fully transferred during the PDMS molding [69]. On the other hand, the low elastic modulus of PDMS ($\approx$ 1.5 MPa) also limits the minimum feature size of the transferable patterns (*i.e.,* ~500 nm) [70,71]. In order to improve the accuracy and resolution, Schmid et al., [72] have developed hPDMS that offers enhanced mechanical properties [73]. Having hybrid PDMS molds allows for reaching a resolution of 10 nm [35], which is the resolution that can be reached by rigid molds. We, therefore, applied hPDMS to the substrate prior to PDMS casting to precisely imprint the submicron pillars from the master mold into the hybrid PDMS replica mold. This hybrid mold was then used in the thermal nanoimprint process thanks to its low deformation and high flexibility. Comparing the dimension of the patterns present on the hybrid PDMS substrate with the original submicron pillars (*i.e.*, those of the master mold) indicated that the deviations in the diameter of the pillars are only 9-10 % while deviations of 3-4 % were observed for the interspacing values.

4.4. Thermal nanoimprint lithography

As PDMS is inert and hydrophobic, there is no need to perform any post-processing on it prior to bringing it into contact with PMMA, and the poor adhesion between PDMS and PMMA is an advantage during the nanoimprint process. After nanoimprinting, optimizing the etching parameters to properly transfer the patterns from PMMA to the final substrate is the key step that affects the feature sizes. Although Pandey et al. [35] have previously shown

the potential of PDMS as the master mold in thermal nanoimprint processes, they did not continue the process to transfer the patterns into the final substrate. In other words, while they transferred the patterns of the PDMS mold to the PMMA layer, which was coated on the final substrate, they did not use the PMMA or any hard mask to etch the final substrate and transfer the patterns into the final substrate. Here, the nanoimprinting process was followed by the proper etching steps to have the desired patterns transferred into the substrate of interest.

The nanoimprinting process parameters, including the applied force, thermoplastic material, embossing temperature, time, and chamber pressure determine the resolution and quality of the transferred patterns. The values reported in the literature for the embossing temperature, while using PMMA as the resist, vary between 120 and 180 °C [74]. At very low temperatures, PMMA is not formable enough to follow the pattern of the master mold, resulting in incomplete pattern transfer or in features that possess a lower aspect ratio than desired. On the contrary, embossing at a very high temperature may crush or destroy the master mold [75]. In our study, the embossing temperature was set to 140 °C. However, PMMA was used as the mask to transfer the submicron pillars first to Cr. Then, the Cr mask was employed to transfer the submicron pillars into the fused silica substrate. Therefore, as long as the height of the submicron pillars formed on PMMA is high enough to etch the unwanted Cr layer, the embossing temperature is not the critical parameter. The applied force and its uniformity are the other crucial parameters to achieve homogeneous and high-resolution patterns throughout the substrate surface and to prevent the mold and its underlying substrate from being damaged. Applying very high forces will damage the hybrid PDMS mold with the degree of mold deformation increasing with the applied force [35]. On the other hand, very low forces result in the nanopatterns not being thoroughly transferred. Achieving full imprinting with high fidelity of the transferred patterns is, therefore, challenging and requires proper optimization of the involved parameters. In our study, 250 N was high enough to fully transfer the submicron pillars into the PMMA without damaging the hybrid PDMS master mold.

Following the above-mentioned process steps led to the realization of high-quality replicas from a single master mold. Inspecting the dimensions and quality of the final patterns transferred into the fused silica substrates (Fig. 5e) and comparing it with the master mold (Fig. 1c) indicates that there are only minor deviations in the diameter and interspacing of the submicron pillars (Table 1). In the case of the submicron pillars with an interspacing of 700 nm, the deviations were around 12% for the diameter and 1% for the interspacing. As for the submicron pillars with an interspacing of 1000 nm, the deviations were around 19% for the diameter and 1% for the interspacing. Considering the fact that the patterned area was relatively large, the effects of such deviations on the patterned area, in its entirety, are not significant. In other words, optimized processing parameters lead to high-fidelity replica molds despite the large number of the steps involved. These results confirm that pattern replication by thermal nanoimprinting produces precisely formed submicron patterns with minimal surface defects.

The primary limitation of the thermal nanoimprint lithography is the process temperature of the master mold, which should be lower than the embossing temperature. Even with this limitation, nanoimprint lithography appears to be the best candidate for decorating the surface of biomaterials with cell-instructive nano/submicron pillars [76].

5. Conclusions

In summary, we developed a precise and facile method for high throughput patterning of various types of surfaces with nanoscale and submicron patterns whose geometries are precisely controlled. First, we used electron beam lithography to fabricate two arrays of submicron pillars with precise dimensions and controlled shape over a large area (3×5 mm^2) of a fused silica substrate. Assessing the adaptation of MC3T3-E1 preosteoblast cells to the fabricated patterns showed that varying the interspacing of the submicron pillars significantly influences the cytoskeletal organization, cell area, cell elongation, and formation of focal adhesions. The interactions of the cells with the submicron pillars were found to be subordinate to the settling state of the cells. The “top state” observed on submicron pillars with an interspacing of 700 nm shifted to a “mixed state” on submicron pillars with an interspacing of 1000 nm, meaning that in the latter, the cells not only interacted with the top of the pillars but also engulfed the whole pillar and came into contact with its lateral sides as well as the substrate. Both types of pillars significantly increased the expression of OPN as compared to a flat control surface. Afterwards, to overcome the restrictions of many fabrication techniques, namely being expensive and time-consuming, we used soft lithography to replicate the submicron pillars present on the original mold into the hybrid PDMS mold. The shape, morphology, and depth of the replicated patterns were analyzed with SEM and FIB, and the results confirmed the geometric fidelity of the hybrid replica. As PDMS is not the material of choice for cell studies, we used hybrid PDMS molds as the master mold in thermal nanoimprint lithography to transfer the patterns to the thermoplastic resist coated on the desired final substrate (fused silica in our study). The results of this study clearly show the advantages of nanoimprint lithography as a unique high-throughput yet precise technique for the patterning of large areas of bio-instructive surfaces, while guarantying the quality and resolution of the nanopatterns required for further biological assessments. The height/depth of the final patterns can be adjusted by optimizing the applied force and embossing temperature as well as through the application of specific etching steps.

Declaration of Competing Interest

The authors declare no conflict of interest.

Acknowledgments

This research has received funding from the European Research Council under the ERC grant agreement no. [677575]. The authors would like to thank Dr. Cornelis W. Hagen (Kees) for the access to the SEM equipment, and Anja van Langen-Suurling for her assistance with the EBL process.

Supplementary materials

Supplementary material associated with this article can be found, in the online version, at doi:10.1016/j.actbio.2021.12.001.

References

[1] Å. Ekblad-Nordberg, L. Walther-Jallow, M. Westgren, C. Götherström, Prenatal stem cell therapy for inherited diseases: past, present, and future treatment strategies: concise review, Stem Cells Transl. Med. (2019).
[2] J. Ng, C.B. Little, S. Woods, S. Whittle, F.Y. Lee, S. Gronthos, S. Mukherjee, D.J. Hunter, D.L. Worthley, Stem cell directed therapies for osteoarthritis: the promise and the practice: concise review, Stem Cells (2019).
[3] L. Zhao, A.D. Kaye, A.J. Kaye, A. Abd-Elsayed, Stem cell therapy for osteonecrosis of the femoral head: current trends and comprehensive review, Curr. Pain Headache Rep. 22 (6) (2018) 41.
[4] M. Ventre, P.A. Netti, Engineering cell instructive materials to control cell fate and functions through material cues and surface patterning, ACS Appl. Mater. Interfaces 8 (24) (2016) 14896–14908.
[5] A. Augello, C. De Bari, The regulation of differentiation in mesenchymal stem cells, Hum. Gene Ther. 21 (10) (2010) 1226–1238.

[6] M. Nouri-Goushki, L. Angeloni, K. Modaresifar, M. Minneboo, P.E. Boukany, M.J. Mirzaali, M.K. Ghatkesar, L.E. Fratila-Apachitei, A.A. Zadpoor, 3D-printed submicron patterns reveal the interrelation between cell adhesion, cell mechanics, and osteogenesis, ACS Appl. Mater. Interfaces 13 (29) (2021) 33767–33781.

[7] K. Modaresifar, S. Azizian, M. Ganjian, L.E. Fratila-Apachitei, A.A. Zadpoor, Bactericidal effects of nanopatterns, a systematic review, Acta Biomaterialia 83 (2019) 29–36, doi:10.1016/j.actbio.2018.09.059.

[8] M. Salandova, I.A.J. van Hengel, I. Apachitei, A.A. Zadpoor, B.C.J. van der Eerden, L.E. Fratila-Apachitei, Inorganic agents for enhanced angiogenesis of orthopedic biomaterials, Adv. Healthc. Mater. 10 (12) (2021) e2002254.

[9] M. Fazel, H.R. Salimijazi, M. Shamanian, M. Minneboo, K. Modaresifar, I.A.J. van Hengel, L.E. Fratila-Apachitei, I. Apachitei, A.A. Zadpoor, Osteogenic and antibacterial surfaces on additively manufactured porous Ti-6Al-4V implants: combining silver nanoparticles with hydrothermally synthesized HA nanocrystals, Mater. Sci. Eng. C Mater. Biol. Appl. 120 (2021) 111745.

[10] H.N. Kim, A. Jiao, N.S. Hwang, M.S. Kim, D.-H. Kim, K.-Y. Suh, Nanotopography-guided tissue engineering and regenerative medicine, Adv. Drug Deliv. Rev. 65 (4) (2013) 536–558.

[11] C.R. Pedrosa, D. Arl, P. Grysan, I. Khan, S.p. Durrieu, S. Krishnamoorthy, M.-C. Durrieu, Controlled nanoscale topographies for osteogenic differentiation of mesenchymal stem cells, ACS Appl. Mater. Interfaces 11 (9) (2019) 8858–8866.

[12] M.J. Dalby, N. Gadegaard, R.O. Oreffo, Harnessing nanotopography and integrin–matrix interactions to influence stem cell fate, Nat. Mater. 13 (6) (2014) 558–569.

[13] S. Dobbenga, L.E. Fratila-Apachitei, A.A. Zadpoor, Nanopattern-induced osteogenic differentiation of stem cells–a systematic review, Acta Biomater. 46 (2016) 3–14.

[14] K. von der Mark, J. Park, S. Bauer, P. Schmuki, Nanoscale engineering of biomimetic surfaces: cues from the extracellular matrix, Cell Tissue Res. 339 (1) (2010) 131.

[15] T. Sjostrom, M.J. Dalby, A. Hart, R. Tare, R.O. Oreffo, B. Su, Fabrication of pillar-like titania nanostructures on titanium and their interactions with human skeletal stem cells, Acta Biomater. 5 (5) (2009) 1433–1441.

[16] L.E. McNamara, T. Sjostrom, K.E. Burgess, J.J. Kim, E. Liu, S. Gordonov, P.V. Moghe, R.M. Meek, R.O. Oreffo, B. Su, M.J. Dalby, Skeletal stem cell physiology on functionally distinct titania nanotopographies, Biomaterials 32 (30) (2011) 7403–7410.

[17] C.-H. Chen, C.-C. Tsai, P.-T. Wu, I.-K. Wang, J. Yu, W.-B. Tsai, Modulation of neural differentiation through submicron-grooved topography surface with modified polydopamine, ACS Appl. Bio. Mater. 2 (1) (2018) 205–216.

[18] S. Watari, K. Hayashi, J.A. Wood, P. Russell, P.F. Nealey, C.J. Murphy, D.C. Genetos, Modulation of osteogenic differentiation in hMSCs cells by submicron topographically-patterned ridges and grooves, Biomaterials 33 (1) (2012) 128–136.

[19] M.J. Dalby, N. Gadegaard, R. Tare, A. Andar, M.O. Riehle, P. Herzyk, C.D. Wilkinson, R.O. Oreffo, The control of human mesenchymal cell differentiation using nanoscale symmetry and disorder, Nat. Mater. 6 (12) (2007) 997–1003.

[20] Y. Sun, C.S. Chen, J. Fu, Forcing stem cells to behave: a biophysical perspective of the cellular microenvironment, Annu. Rev. Biophys. 41 (2012) 519–542.

[21] M. Ganjian, K. Modaresifar, M.R. Ligeon, L.B. Kunkels, N. Tümer, L. Angeloni, C.W. Hagen, L.G. Otten, P.-L. Hagedoorn, I. Apachitei, L.E. Fratila-Apachitei, A.A. Zadpoor, Nature helps: toward bioinspired bactericidal nanopatterns, Advanced Materials Interfaces 6 (16) (2019) 1900640, doi:10.1002/admi.201900640.

[22] K. Modaresifar, L.B. Kunkels, M. Ganjian, N. Tümer, C.W. Hagen, L.G. Otten, P.-L. Hagedoorn, L. Angeloni, M.K. Ghatkesar, L.E. Fratila-Apachitei, A.A. Zadpoor, Deciphering the roles of interspace and controlled disorder in the bactericidal properties of nanopatterns against Staphylococcus aureus, Nanomaterilas 10 (2) (2020) 347, doi:10.3390/nano10020347.

[23] D.S. Widyaratih, P.-L. Hagedoorn, L.G. Otten, M. Ganjian, N. Tümer, I. Apachitei, C.W. Hagen, L.E. Fratila-Apachitei, A.A. Zadpoor, Towards osteogenic and bactericidal nanopatterns? Nanotechnology 30 (20) (2019) 20LT01.

[24] D.K. Oh, H. Jeong, J. Kim, Y. Kim, I. Kim, J.G. Ok, J. Rho, Top-down nanofabrication approaches toward single-digit-nanometer scale structures, J. Mech. Sci. Technol. 35 (3) (2021) 837–859.

[25] M.N. M.N.U. Hashim, M. Md Arshad, A.R. Ruslinda, S. Rahman, M. Fathil, M.H. Ismail, Top-down nanofabrication and characterization of 20 nm silicon nanowires for biosensing applications, Plos One 11 (3) (2016) e0152318, doi:10.1371/journal.pone.0152318.

[26] M. Nouri-Goushki, M.J. Mirzaali, L. Angeloni, D. Fan, M. Minneboo, M.K. Ghatkesar, U. Staufer, L.E. Fratila-Apachitei, A.A. Zadpoor, 3d printing of large areas of highly ordered submicron patterns for modulating cell behavior, ACS Applied Materials and Interfaces 12 (1) (2019) 200–208, doi:10.1021/acsami.9b17425.

[27] M. Ganjian, K. Modaresifar, H. Zhang, P.-L. Hagedoorn, L.E. Fratila-Apachitei, A.A. Zadpoor, Reactive ion etching for fabrication of biofunctional titanium nanostructures, Scientific Reports 9 (1) (2019) 1–20, doi:10.1038/s41598-019-55093-y.

[28] E.P. Ivanova, J. Hasan, H.K. Webb, G. Gervinskas, S. Juodkazis, V.K. Truong, A.H.F. Wu, R.N. Lamb, V.A. Baulin, G.S. Watson, J.A. Watson, D.E. Mainwaring, R.J. Crawford, Bactericidal activity of black silicon, Nature Communications 4 (1) (2013) 1–7, doi:10.1038/ncomms3838.

[29] F. Hizal, I. Zhuk, S. Sukhishvili, H.J. Busscher, H.C. van der Mei, C.-H. Choi, interfaces, Impact of 3D hierarchical nanostructures on the antibacterial efficacy of a bacteria-triggered self-defensive antibiotic coating, ACS Applied Materials and Interfaces 7 (36) (2015) 20304–20313, doi:10.1021/acsami.5b05947.

[30] G. Yi, Y. Yuan, X. Li, Y. Zhang, ZnO nanopillar coated surfaces with substrate-dependent superbactericidal property, Small 14 (14) (2018) 1703159, doi:10.1002/smll.201703159.

[31] P.M. Tsimbouri, L. Fisher, N. Holloway, T. Sjostrom, A. Nobbs, R.D. Meek, B. Su, M.J. Dalby, Osteogenic and bactericidal surfaces from hydrothermal titania nanowires on titanium substrates, Scientific Reports 6 (1) (2016) 1–12, doi:10.1038/srep36857.

[32] A. Jaggessar, A. Mathew, H. Wang, T. Tesfamichael, C. Yan, P.K. Yarlagadda, Mechanical, bactericidal and osteogenic behaviours of hydrothermally synthesised TiO2 nanowire arrays, Journal of the Mechanical Behavior of Biomedical Materials 80 (2018) 311–319, doi:10.1016/j.jmbbm.2018.02.011.

[33] S.H. Ahn, L.J. Guo, Large-area roll-to-roll and roll-to-plate nanoimprint lithography: a step toward high-throughput application of continuous nanoimprinting, ACS Nano 3 (8) (2009) 2304–2310.

[34] S.H. Ahn, L.J. Guo, High-speed roll-to-roll nanoimprint lithography on flexible plastic substrates, Adv. Mater. 20 (11) (2008) 2044–2049.

[35] A. Pandey, S. Tzadka, D. Yehuda, M. Schvartzman, Soft thermal nanoimprint with a 10 nm feature size, Soft Matter 15 (13) (2019) 2897–2904.

[36] A. Jaggessar, H. Shahali, A. Mathew, P. Yarlagadda, Bio-mimicking nano and micro-structured surface fabrication for antibacterial properties in medical implants, J. Nanobiotechnol. 15 (1) (2017) 64.

[37] H. Su, X.R. Cheng, T. Endo, K. Kerman, Photonic crystals on copolymer film for label-free detection of DNA hybridization, Biosens. Bioelectron. 103 (2018) 158–162.

[38] J. Ahn, S. Kwon, S. Jung, W.S. Lee, J. Jeong, H. Lim, Y.B. Shin, J. Lee, Fabrication of pyrrole-based electrochemical biosensor platform using nanoimprint lithography, Adv. Mater. Interfaces 5 (8) (2018) 1701593.

[39] M. Vaisman, N. Jain, Q. Li, K.M. Lau, E. Makoutz, T. Saenz, W.E. McMahon, A.C. Tamboli, E.L. Warren, GaAs solar cells on nanopatterned Si substrates, IEEE J. Photovoltaics 8 (6) (2018) 1635–1640.

[40] W.-C. Tsao, Q.-C. Zeng, Y.-H. Yeh, C.-H. Tsai, H.-F. Hong, C.-Y. Chen, T.-Y. Lin, Y.-Y. Huang, C.-W. Tsao, J.-W. Pan, Efficiency evaluation of a hybrid miniaturized concentrated photovoltaic for harvesting direct/diffused solar light, J. Opt. (2019).

[41] F. Viela, I. Navarro-Baena, J.J. Hernández, M.R. Osorio, I. Rodríguez, Moth–eye mimetic cytocompatible bactericidal nanotopography: a convergent design, Bioinspiration Biomimetics 13 (2) (2018) 026011.

[42] F. Kantawong, K.E. Burgess, K. Jayawardena, A. Hart, R.J. Burchmore, N. Gadegaard, R.O. Oreffo, M.J. Dalby, Whole proteome analysis of osteoprogenitor differentiation induced by disordered nanotopography and mediated by ERK signalling, Biomaterials 30 (27) (2009) 4723–4731.

[43] J.R. Wang, S.F. Ahmed, N. Gadegaard, R.D. Meek, M.J. Dalby, S.J. Yarwood, Nanotopology potentiates growth hormone signalling and osteogenesis of mesenchymal stem cells, Growth Horm. IGF Res. 24 (6) (2014) 245–250.

[44] M.J. Dalby, N. Gadegaard, R. Tare, A. Andar, M.O. Riehle, P. Herzyk, C.D. Wilkinson, R.O. Oreffo, The control of human mesenchymal cell differentiation using nanoscale symmetry and disorder, Nat. Mater. 6 (12) (2007) 997–1003.

[45] S. Li, D. Chu, A review of thin-film transistors/circuits fabrication with 3D self-aligned imprint lithography, Flexible Printed Electron. 2 (1) (2017) 013002.

[46] Z. Wang, P. Yi, L. Peng, X. Lai, J. Ni, Continuous fabrication of highly conductive and transparent ag mesh electrodes for flexible electronics, IEEE Trans. Nanotechnol. 16 (4) (2017) 687–694.

[47] X. Gao, Y. Huang, X. He, X. Fan, Y. Liu, H. Xu, D. Wu, C. Wan, Mechanically enhanced electrical conductivity of polydimethylsiloxane-based composites by a hot embossing process, Polymers 11 (1) (2019) 56.

[48] S. Callens, D. Fan, I. van Hengel, M. Minneboo, L.E. Fratila-Apachitei, A.A. Zadpoor, Emergent collective organization of bone cells in complex curvature fields, bioRxiv (2020).

[49] U. Horzum, B. Ozdil, D.J.M. Pesen-Okvur, Step-by-step quantitative analysis of focal adhesions, MethodsX 1 (2014) 56–59.

[50] V. Bhingardive, L. Menahem, M. Schvartzman, Soft thermal nanoimprint lithography using a nanocomposite mold, Nano Res. 11 (5) (2018) 2705–2714.

[51] K.L. Lai, M.H. Hon, I.C. Leu, Pattern formation on polymer resist by solvent-assisted nanoimprinting with PDMS mold as a solvent transport medium, J. Micromech. Microeng. 21 (7) (2011).

[52] W.-X. Su, C.-Y. Wu, Y.-C. Lee, Anti-reflection nano-structures fabricated on curved surface of glass lens based on metal contact printing lithography, Microelectron. Eng. 214 (2019) 15–20.

[53] M.D. Cabezas, B. Meckes, C.A. Mirkin, M. Mrksich, Subcellular control over focal adhesion anisotropy, independent of cell morphology, dictates stem cell fate, ACS Nano 13 (10) (2019) 11144–11152.

[54] M. Bao, J. Xie, A. Piruska, W.T.S. Huck, 3D microniches reveal the importance of cell size and shape, Nature Communications 8 (1) (2017) 1–12.

[55] F. Jiao, Y. Zhao, Q. Sun, B. Huo, Spreading area and shape regulate the apoptosis and osteogenesis of mesenchymal stem cells on circular and branched micropatterned islands, Journal of Biomedical Materials Research 108 (10) (2020) 2080–2089, doi:10.1002/jbm.a.36967.

[56] A. Ron, E.U. Azeloglu, R.C. Calizo, M. Hu, S. Bhattacharya, Y. Chen, G. Jayaraman, S. Lee, S.R. Neves-Zaph, H. Li, Cell shape information is transduced through tension-independent mechanisms, Nat. Commun. 8 (1) (2017) 1–15.

[57] H. Seong, S.G. Higgins, J. Penders, J.P. Armstrong, S.W. Crowder, A.C. Moore, J.E. Sero, M. Becce, M.M. Stevens, Size-tunable nanoneedle arrays for influencing stem cell morphology, gene expression, and nuclear membrane curvature, ACS Nano 14 (5) (2020) 5371–5381.

[58] K. Modaresifar, M. Ganjian, L. Angeloni, M. Minneboo, M.K. Ghatkesar, P.L. Hagedoorn, L.E. Fratila-Apachitei, A.A. Zadpoor, On the use of black ti as a bone substituting biomaterial: behind the scenes of dual-functionality, Small (2021) 2100706.
[59] F. Viela, D. Granados, A. Ayuso-Sacido, I. Rodríguez, Biomechanical cell regulation by high aspect ratio nanoimprinted pillars, Adv. Funct. Mater. 26 (31) (2016) 5599–5609.
[60] C.W. Kuo, D.-Y. Chueh, P. Chen, Investigation of size–dependent cell adhesion on nanostructured interfaces, J. Nanobiotechnol. 12 (1) (2014) 1–10.
[61] F. Viela, D. Granados, A. Ayuso-Sacido, I. Rodríguez, Biomechanical cell regulation by high aspect ratio nanoimprinted pillars, Adv. Funct. Mater. 26 (31) (2016) 5599–5609.
[62] S.G. Higgins, M. Becce, A. Belessiotis-Richards, H. Seong, J.E. Sero, M.M. Stevens, High-aspect-ratio nanostructured surfaces as biological metamaterials, Adv. Mater. 32 (9) (2020) e1903862.
[63] J. Hasan, S. Jain, K. Chatterjee, Nanoscale topography on black titanium imparts multi-biofunctional properties for orthopedic applications, Sci. Rep. 7 (2017) 41118.
[64] A. Ray, O. Lee, Z. Win, R.M. Edwards, P.W. Alford, D.-H. Kim, P.P. Provenzano, Anisotropic forces from spatially constrained focal adhesions mediate contact guidance directed cell migration, Nat. Commun. 8 (1) (2017) 1–17.
[65] M. Werner, S.B. Blanquer, S.P. Haimi, G. Korus, J.W. Dunlop, G.N. Duda, D.W. Grijpma, A. Petersen, Surface curvature differentially regulates stem cell migration and differentiation via altered attachment morphology and nuclear deformation, Adv. Sci. 4 (2) (2017) 1600347.
[66] S.G. Higgins, M. Becce, A. Belessiotis-Richards, H. Seong, J.E. Sero, M.M. Stevens, High-aspect-ratio nanostructured surfaces as biological metamaterials, Adv. Mater. (2020) 1903862.
[67] D. Quéré, Wetting and roughness, Annual Review of Materials Research 38 (2008) 71–99, doi:10.1146/annurev.matsci.38.060407.132434.
[68] N. Vrancken, S. Sergeant, G. Vereecke, G. Doumen, F. Holsteyns, H. Terryn, S. De Gendt, X. Xu, Superhydrophobic breakdown of nanostructured surfaces characterized in situ using ATR–FTIR, Langmuir 33 (15) (2017) 3601–3609, doi:10.1021/acs.langmuir.6b04471.
[69] E. Baquedano, R.V. Martinez, J.M. Llorens, P.A. Postigo, Fabrication of silicon nanobelts and nanopillars by soft lithography for hydrophobic and hydrophilic photonic surfaces, Nanomaterials 7 (5) (2017) 109.
[70] T.W. Odom, J.C. Love, D.B. Wolfe, K.E. Paul, G.M. Whitesides, Improved pattern transfer in soft lithography using composite stamps, Langmuir 18 (13) (2002) 5314–5320.
[71] C. Masciullo, A. Sonato, F. Romanato, M. Cecchini, Perfluoropolyether (PFPE) intermediate molds for high-resolution thermal nanoimprint lithography, Nanomaterials 8 (8) (2018) 609, doi:10.3390/nano8080609.
[72] H. Schmid, B. Michel, Siloxane polymers for high-resolution, high-accuracy soft lithography, Macromolecules 33 (8) (2000) 3042–3049.
[73] C. Zheng, Nanofabrication: principles, capabilities, and limits, Springer, 2016.
[74] A. Shamsi, A. Amiri, P. Heydari, H. Hajghasem, M. Mohtashamifar, M. Esfandiari, Low cost method for hot embossing of microstructures on PMMA by SU-8 masters, Microsyst. Technol. 20 (10–11) (2013) 1925–1931.
[75] M. Kim, B.-U. Moon, C.H. Hidrovo, Enhancement of the thermo-mechanical properties of PDMS molds for the hot embossing of PMMA microfluidic devices, J. Micromech. Microeng. 23 (9) (2013) 095024.
[76] J. Chen, J. Shi, A. Cattoni, D. Decanini, Z. Liu, Y. Chen, A.-M. Haghiri-Gosnet, A versatile pattern inversion process based on thermal and soft UV nanoimprint lithography techniques, Microelectron. Eng. 87 (5–8) (2010) 899–903.